



## OPEN ACCESS

EDITED BY  
Lauri Holappa,  
University of Oulu, Finland

REVIEWED BY  
Binbin Ni,  
Wuhan University, China  
Nickolay Ivchenko,  
Royal Institute of Technology, Sweden

\*CORRESPONDENCE  
Emma Bland,  
emmob@unis.no

SPECIALTY SECTION  
This article was submitted to Space  
Physics,  
a section of the journal  
Frontiers in Astronomy and Space  
Sciences

RECEIVED 25 June 2022  
ACCEPTED 12 August 2022  
PUBLISHED 06 September 2022

CITATION  
Bland E, Bozóki T and Partamies N  
(2022), Spatial extent of the energetic  
electron precipitation region  
during substorms.  
*Front. Astron. Space Sci.* 9:978371.  
doi: 10.3389/fspas.2022.978371

COPYRIGHT  
© 2022 Bland, Bozóki and Partamies.  
This is an open-access article  
distributed under the terms of the  
[Creative Commons Attribution License  
\(CC BY\)](https://creativecommons.org/licenses/by/4.0/). The use, distribution or  
reproduction in other forums is  
permitted, provided the original  
author(s) and the copyright owner(s) are  
credited and that the original  
publication in this journal is cited, in  
accordance with accepted academic  
practice. No use, distribution or  
reproduction is permitted which does  
not comply with these terms.

# Spatial extent of the energetic electron precipitation region during substorms

Emma Bland<sup>1\*</sup>, Tamás Bozóki<sup>2,3</sup> and Noora Partamies<sup>1,4</sup>

<sup>1</sup>Department of Arctic Geophysics, University Centre in Svalbard, Longyearbyen, Norway, <sup>2</sup>Institute of Earth Physics and Space Science (ELKH EPSS), Sopron, Hungary, <sup>3</sup>Department of Optics and Quantum Electronics, University of Szeged, Szeged, Hungary, <sup>4</sup>Birkeland Centre for Space Science, University of Bergen, Bergen, Norway

The spatial coverage of the energetic electron precipitation (EEP) region during three substorms has been determined using a combination of ground-based instruments in North America. The primary datasets used to determine the presence or absence of EEP are riometer measurements of cosmic noise absorption (CNA); attenuation of the 10–11 MHz atmospheric noise in the D-region ionosphere determined using the Super Dual Auroral Radar Network (SuperDARN); amplitude variations in subionospheric very low frequency (VLF) propagation observed using the Antarctic-Arctic Radiation-belt (Dynamic) Deposition VLF Atmospheric Research Konsortium (AARDDVARK) VLF receivers, and total electron content measurements derived from global navigation satellite systems. Our results show that substorm EEP during moderate geomagnetic conditions can extend considerably equatorward or poleward of the average latitude limits reported in a previous statistical study of substorm EEP and an EEP model. This evidence is provided by the SuperDARN radars and the radar signature is not always accompanied by cosmic noise absorption measured by the riometers. Further work is required to determine which EEP energies and fluxes the SuperDARN radars are sensitive to, but we can conclude that EEP with sufficient flux to attenuate 10–11 MHz radiowaves by ~5 dB reaches latitudes well equatorward of the statistical EEP latitude limits previously modelled for > 30 keV electrons.

## KEYWORDS

particle precipitation, substorm, ionosphere, riometer, superdarn

## 1 Introduction

Substorms are one of the key processes that facilitate energy transfer from the Earth's magnetotail into the ionosphere through energetic electron precipitation (EEP). At the substorm onset, there is an injection of energetic electrons from the plasma sheet into a narrow spatial region of the auroral zone ionosphere, which then rapidly expands azimuthally and poleward (e.g., [Berkey et al., 1974](#); [Gjerloev et al., 2007](#); [Spanwick et al., 2009](#)). The particle injection is often observed as a sharp increase in cosmic noise absorption (CNA), and this decays gradually throughout the expansion and recovery

phases (e.g., Spanswick et al., 2007; Partamies et al., 2021). The peak CNA is associated with precipitating electron energies of about 40–60 keV (Kellerman et al., 2015), which impact the atmosphere at about 90 km altitude (Fang et al., 2008).

Precipitating electrons that reach altitudes below about 120 km are known to affect the atmospheric chemistry through the production of odd-nitrogen ( $\text{NO}_x = \text{N}, \text{NO}, \text{NO}_2$ ) and odd-hydrogen ( $\text{HO}_x = \text{H}, \text{OH}, \text{HO}_2$ ) chemical species, which are catalysts in ozone depletion reactions (Sinnhuber et al., 2012).  $\text{HO}_x$  species are produced mainly in the mesosphere due to medium-energy electron precipitation (tens of keV), while  $\text{NO}_x$  species are produced mainly in the thermosphere due to auroral electron precipitation with energies of ~1–10 keV. The short chemical lifetime of  $\text{HO}_x$  species limits their atmospheric impact to the mesosphere. In contrast,  $\text{NO}_x$  species have a long chemical lifetime in the dark and can be transported downwards in the polar vortex, leading to ozone depletion in the mesosphere and stratosphere. These atmospheric chemical effects have been identified during individual EEP events (e.g., Daae et al., 2012; Turunen et al., 2016; Smith-Johnsen et al., 2018) and as a contributor to natural climate variability (e.g., Randall et al., 2007; Seppälä et al., 2007; Seppälä et al., 2014). To help quantify these contributions, substantial effort has gone into developing realistic statistical descriptions of the EEP forcing for climate modelling applications. This includes the van de Kamp et al. (2016), van de Kamp et al. (2018) models of > 30 keV electron flux, which are derived from long-term electron flux measurements from the Polar Orbiting Environmental Satellites (POES) and parametrised by the geomagnetic indices  $A_p$  and  $Dst$ . Geomagnetic indices provide the long time series of geomagnetic activity that is necessary for long-term modelling of the Earth's climate, but one should be aware that this approach systematically excludes some components of the EEP forcing. For example, a very common feature of the substorm recovery phase is pulsating aurora, which is associated with the high-energy tail of the auroral precipitation spectrum and persists for several hours after the magnetic signature has recovered (Partamies et al., 2017). This type of aurora has occurrence rates exceeding 40% in the early morning sector (Jones et al., 2011; Bland et al., 2019) and is known to cause ozone depletion in the auroral oval (Turunen et al., 2016; Tesema et al., 2020; Verronen et al., 2021). It is therefore likely that the  $A_p$  and  $Dst$  parametrisations of EEP do not properly capture the energy input associated with pulsating aurora during substorm recovery phases.

Global geomagnetic indices with time resolutions of hours or days are also unable to capture the variability in the EEP energy spectrum, spatial extent, and temporal evolution of EEP from event to event. The  $A_p$  index, for example, provides only a daily average of geomagnetic activity and could therefore underestimate or overestimate the energy input from substorm EEP. The 3-h time resolution of the  $a_p$  (or  $Kp$ ) index is comparable to the typical substorm duration of 2–4 h,

so this may still be insufficient to describe the EEP input. Recently, Sergeev et al. (2020) developed a semi-empirical model that characterises the recurring spatial and temporal features of auroral absorption during substorms. This model is driven by the recently-developed midlatitude positive bay index, which captures the field-aligned current enhancement from the substorm current wedge (McPherron and Chu, 2018). Although accounting for this variability may be unnecessary for climate modelling, it is important in space weather applications because the amount of auroral absorption depends strongly on the current state and time history of the magnetosphere–ionosphere system. Chemical changes in the middle atmosphere due to EEP also depend heavily on the strength and duration of the forcing (Tesema et al., 2020), so long-term average particle energy spectra may not be sufficient for describing the short-term atmospheric response.

To work towards a more complete description of the variability in EEP during substorms, we use a combination of ground-based instruments to study the spatial and temporal evolution of the EEP impact area for three substorms that occurred during moderate geomagnetic conditions ( $10 \leq A_p \leq 25$ ). We use the Go-Canada riometer network (Spanswick et al., 2007), the Super Dual Auroral Radar Network (SuperDARN) (Greenwald et al., 1995; Chisham et al., 2007; Nishitani et al., 2019), the network of very low frequency (VLF) receivers that comprise the Antarctic-Arctic Radiation-belt (Dynamic) Deposition VLF Atmospheric Research Konsortium (AARDDVARK) (Clilverd et al., 2009), and vertical total electron content measurements derived from global navigation satellite systems (Rideout and Coster, 2006). The spatial extent of the EEP region for each substorm is then compared with the van de Kamp et al. (2018) model prediction, and an earlier statistical study of the latitudinal extent of substorm EEP performed using satellite measurements of particle energy spectra (Cresswell-Moorcock et al., 2013). These results provide some insight into how well the geomagnetic index  $A_p$  captures the spatial coverage of substorm EEP, and how well the average latitude limits of > 30 keV electron flux determined by Cresswell-Moorcock et al. (2013) match the substorm EEP region determined from the ground-based instruments. Our results provide a detailed picture of the two-dimensional spatial evolution of substorm EEP at the energy ranges that are associated with auroral absorption and ozone depletion.

## 2 Instrumentation

The locations and fields of view of the main instruments used in this study are shown in Table 1 and Figure 1. Dashed lines in Figure 1 indicate altitude-adjusted corrected geomagnetic (AACGM) coordinates (Shepherd, 2014) projected to a height of 100 km. The Go-Canada riometer network consists of 14 wide-beam ( $60^\circ$ ) riometers that measure the absorption of 30 MHz cosmic radio noise.

**TABLE 1** Station codes and locations of the riometers, SuperDARN radars, and VLF transmitters and receivers used in this study. AACGM = Altitude-Adjusted Corrected Geomagnetic. MLT = magnetic local time.

Station code	Name	Geodetic latitude	Geodetic longitude	AACGM latitude	AACGM longitude	L Value	MLT at 00UT
<i>Riometers</i>							
CHUR	Churchill	58.76	-94.08	67.57	-24.49	6.9	17.6
DAWS	Dawson	64.05	-139.11	65.92	-83.39	6.0	13.7
FSIM	Fort Simpson	61.76	-121.23	66.97	-62.99	6.5	15.1
FSMI	Fort Smith	60.02	-111.95	66.86	-50.57	6.5	15.9
GILL	Gillam	56.38	-94.64	65.31	-25.04	5.7	17.6
ISLL	Island Lake	53.86	-94.66	62.94	-24.81	4.8	17.6
MCMU	Fort McMurray	56.66	-111.21	63.76	-48.54	5.1	16.0
PGEO	Prince George	53.81	-122.83	58.93	-61.92	3.8	15.1
PINA	Pinawa	50.02	-96.04	59.21	-26.47	3.8	17.5
RABB	Rabbit Lake	58.22	-103.68	66.27	-38.62	6.2	16.7
RANK	Rankin Inlet	62.82	-92.11	71.42	-21.99	9.8	17.8
TALO	Taloyoak	69.54	-93.55	77.49	-26.05	21.3	17.5
<i>SuperDARN Radars</i>							
CLY	Clyde River	70.49	-68.50	77.41	17.36	21.0	20.4
GBR	Goose Bay	53.32	-60.46	59.49	23.13	3.9	20.8
INV	Inuvik	68.41	-133.77	71.18	-81.04	9.6	13.9
KAP	Kapuskasing	49.39	-82.32	58.72	-6.58	3.7	18.8
PGR	Prince George	53.98	-122.59	59.15	-61.69	3.8	15.1
RKN	Rankin Inlet	62.83	-92.11	71.43	-22.00	9.9	17.8
SAS	Saskatoon	52.16	-106.53	60.13	-41.29	4.0	16.5
<i>VLF transmitters</i>							
NDK		46.37	-98.34	55.38	-29.38	3.1	17.3
NLK		48.20	-121.92	53.45	-59.34	2.8	15.3
<i>VLF receivers</i>							
CHU	Churchill	58.73	-94.05	67.48	-24.43	6.8	17.6
NYA	Ny Ålesund	78.92	11.93	76.65	106.47	18.8	2.4
REY	Reykjavik	64.13	-21.93	64.19	64.38	5.3	23.6
SEA	Seattle	47.95	-124.38	52.70	-62.02	2.7	15.1

The locations of the riometers used in this study are shown as grey circles in [Figure 1](#). The symbol size is the same for all riometers and indicates the approximate field of view projected to 90 km height. The cosmic noise absorption (CNA) is measured relative to a 'quiet day curve' (QDC) that characterises the background sidereal variation of the cosmic noise strength during undisturbed conditions. Deviations from the QDC are attributed to absorption of the cosmic noise through collisions between neutrals and free electrons, so an increase in the electron density due to EEP can be identified as an increase in CNA. The ionospheric electron density and the electron-neutral collision frequency are typically most favourable for attenuating HF radiowaves at about 90 km altitude (e.g., [Rodger et al., 2012](#)), so changes in CNA are associated with EEP energies exceeding 30 keV.

To extend the spatial coverage provided by the riometers, we use raw power measurements from several SuperDARN radars in North America ([Super Dual Auroral Radar Network, 2021](#); [Super Dual Auroral Radar Network, 2022](#)). The near-range fields of view of the SuperDARN radars used in this study are represented by the blue fan-shaped symbols in [Figure 1](#). SuperDARN radars are phased-array high frequency (HF) radar systems consisting of a linear array of log-periodic or twin-terminated folded dipole antennas. The standard SuperDARN field of view extends to over 3,500 km in range, but in this study we consider only the very near-range field of view that covers the D-region ionosphere (e.g., [Bland et al., 2021](#)). The field of view is divided into 16 azimuthal beams that are sampled in succession. For this study we use data only from the beam that is shaded dark blue in the figure, which is

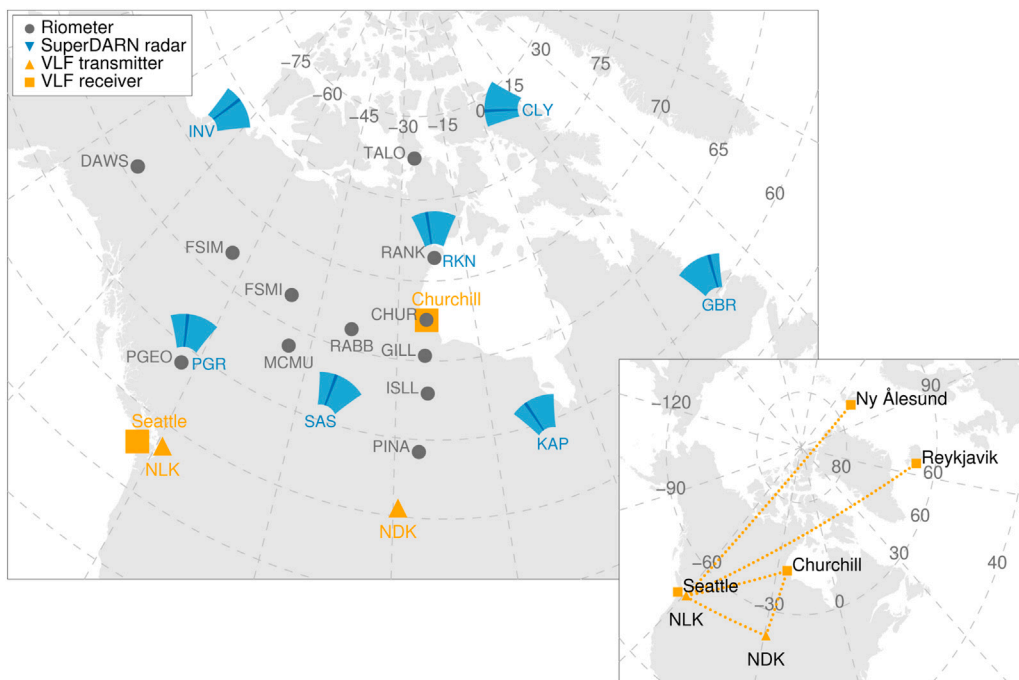


**FIGURE 1**

Locations and fields of view of the riometers, SuperDARN radars, and VLF transmitters and receivers used in this study. For the SuperDARN radars, only the near-range field of view is shown, and the shading indicates the beam direction that was used (see text for details). The propagation paths between selected VLF transmitter–receiver pairs are shown in the inset.

beam 12 for the GBR radar and beam 5 for all other radars. Building on results from our earlier work (Bland et al., 2018; Bland et al., 2019), we use a riometry-like approach to estimate the attenuation of the 10–11 MHz radio noise at each SuperDARN radar site. At this frequency range, radio noise arises primarily from radio emissions associated with lightning activity (atmospheric noise), as well as anthropogenic sources such as radio emissions from electrical equipment and interference from other HF transmitters (Ponomarenko et al., 2022). These noise sources are therefore distinct from the cosmic noise that riometers are sensitive to. To distinguish these measurements from the 30 MHz CNA, we refer to the attenuation of the 10–11 MHz noise measured by the SuperDARN radars as *atmospheric noise attenuation* (ANA). Our earlier work shows that the SuperDARN radars have sufficient sensitivity to detect ANA associated with relatively low-flux EEP during pulsating aurora (Bland et al., 2019; Bland et al., 2021), so this method is also appropriate for detecting substorm EEP.

Also shown in Figure 1 are four VLF receivers from the AARDDVARK network and the powerful VLF communication transmitters NDK and NLK. The propagation paths between selected transmitter and receiver sites are shown in the figure inset. AARDDVARK measures amplitude and phase variations of the narrowband VLF radiowaves along these paths. VLF waves

propagate within the Earth–ionosphere waveguide, and any change in the height of the D-region ionospheric boundary caused by EEP can be observed by a VLF receiver as a decrease in amplitude (increase in phase) (Clilverd et al., 2008). At night time the reflection height for the VLF propagation is expected to be about 85 km, so the VLF data provide information about a higher energy range of precipitating electrons compared to the riometer and radar observations, from about 50 keV to over 200 keV (Rodger et al., 2012).

In addition to the instruments shown in Figure 1, we also use vertically-integrated total electron content (vTEC) measurements derived from the World-wide Global Navigation Satellite Systems Receiver Network to validate the EEP impact area determined from the radio instruments described above. The high density and wide spatial coverage of the vTEC dataset complements the relatively sparse measurements from the other radio instruments. The processed vTEC dataset (Coster, 2019) is binned in a 1° geographic latitude by 1° longitude grid. Although the vTEC measurements do not provide any height or energy information about the EEP, a comparison between vTEC and CNA measurements during two substorms by Watson et al. (2011) showed that 1 dB of CNA is associated with an increase in vTEC of about 2–4 TECu, whereas lower-energy EEP impacting the F-region ionosphere produce much larger changes up to 15 TECu (Mendillo, 2006).

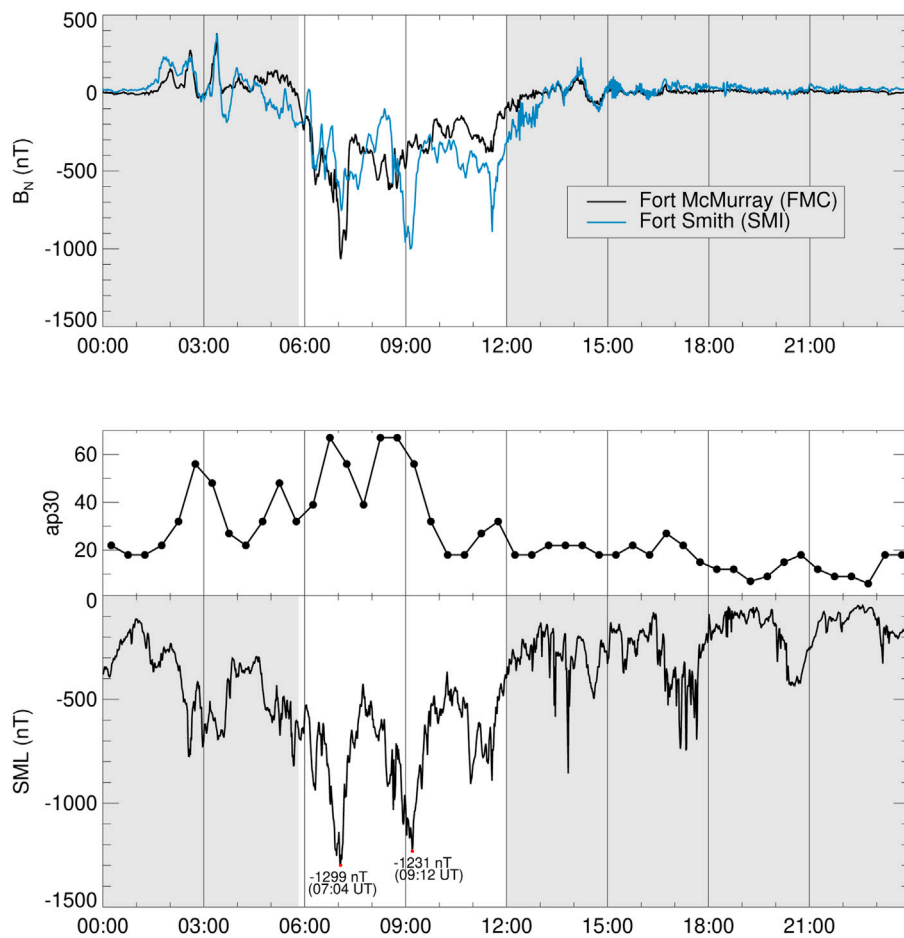


**FIGURE 2**

Magnetic field disturbances and selected geomagnetic indices for 25 October 2019. The top panel shows the magnetic field disturbance in the local magnetic north direction,  $B_N$  measured by the Fort McMurray (FMC) and Fort Smith (SMI) magnetometers. The centre and bottom panels show the  $ap_{30}$  and SML indices respectively.

To obtain an overview of the ground magnetic field disturbance during the substorms, we use the gridded magnetic field data product from SuperMAG (Gjerloev, 2012), which provides ground magnetic field vectors on an equal area magnetic coordinate grid. We also use the data from two individual magnetometers at Fort McMurray and Fort Smith, which are part of the CARISMA magnetometer network (Mann et al., 2008). Several geomagnetic indices are also used to describe the substorm evolution. These are: the lower component of the auroral electrojet index derived from SuperMAG, known as SML (Newell and Gjerloev, 2011); the daily geomagnetic index  $Ap$ , which is the daily average of the eight 3-h  $ap$  indices (Matzka et al., 2021a; Matzka et al., 2021b); and  $ap_{30}$ , which is like the  $ap$  index but provided with a time resolution of 30 min (Matzka et al., 2022; Yamazaki et al., 2022).

### 3 Substorm on 25 October 2019

Our main substorm case study event occurred on 25 October 2019. The top panel of Figure 2 shows the magnetic field disturbance in the local magnetic north direction,  $B_N$ , measured by the Fort McMurray (FMC) and Fort Smith (SMI) magnetometers. These instruments are co-located with the MCMU and FSMI riometers (see Table 1). We identify the substorm onset by the sudden decrease in  $B_N$  at FMC at 05:49 UT. The substorm consists of three intensifications with local  $B_N$  minima at 07:04 UT (FMC), 09:12 UT (SMI) and 11:36 UT (SMI), and the recovery phase ends at approximately 12:00 UT. In the lower panels of Figure 2 we show the  $ap_{30}$  index and the SML index. Both  $ap_{30}$  and SML capture the main features of the magnetic field disturbance detected by the individual FMC and SMI magnetometers.

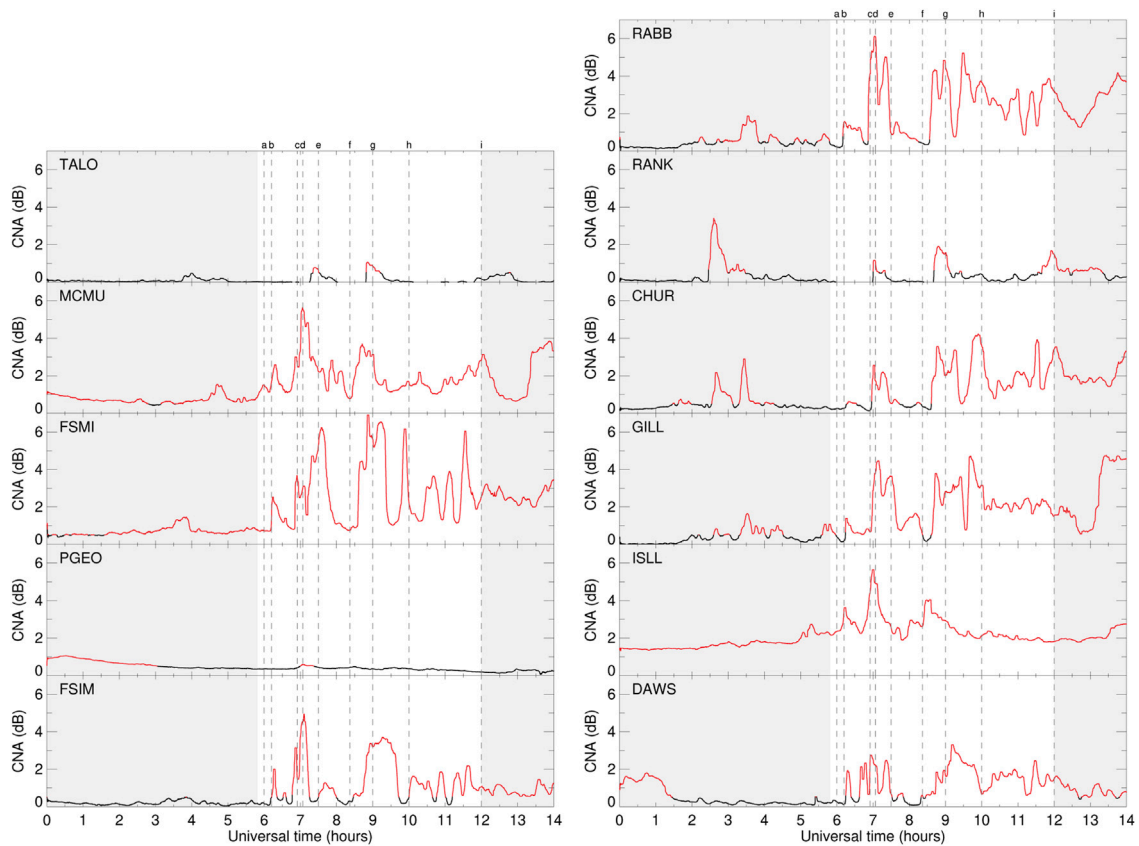


**FIGURE 3**

30 MHz cosmic noise absorption (CNA) measurements from the Go-Canada riometer network on 25 October 2019. CNA measurements below the threshold value of 0.5 dB are coloured black. The vertical dashed lines correspond to the time intervals shown in [Figure 7](#).

### 3.1 Cosmic noise absorption

The CNA measurements from the Go-Canada riometer network are shown in [Figure 3](#). We determined the QDC for each riometer using the raw voltage measurements obtained during the 21-day period centered on the substorm event day (15 October to 4 November 2019). The most active days during this time interval are the event day and the day after (25–26 October), and there were no major solar flares or solar proton events. To construct the QDC for each riometer, the raw data were organised into 30 min bins of sidereal time, and then the 90th percentile value in each bin was selected as the quiet day voltage. This percentile-based method appears to accurately characterise the quiet-time voltage measurements within the 21-days interval without being significantly impacted by the data from more active days. We then calculated the CNA relative to the QDC as

$$\text{CNA (dB)} = \log_{10} \left( \frac{V}{V_0} \right) \quad (1)$$

where  $V$  is the measured voltage from the riometer and  $V_0$  is the value of the quiet day curve in the corresponding sidereal

time bin. The resulting CNA estimates for each riometer are shown in [Figure 3](#). To remove short-duration fluctuations, we also smoothed the data using a boxcar filter of width 1 h. The line colour is red when the CNA exceeds 0.5 dB, which we have determined to be the threshold amount of CNA that can be reliably measured using this dataset. CNA estimates below this threshold are shown in black. Note that there is a 1.3 dB offset in the ISLL data that is probably caused by an instrumental artifact and will be corrected manually later. The vertical dashed lines correspond to specific time intervals during the substorm that will be discussed later. The left column shows the data from the north-south chain of riometers, and the data from the other riometers are shown in the right column in order of east (top) to west (bottom). Most riometers detect a CNA enhancement at around 07:00 UT, which corresponds to the first intensification measured by the magnetometers ([Figure 2](#)). The CNA enhancement occurs about 30 min later at TALO, indicating a poleward expansion of the EEP region. A second CNA enhancement is observed by most riometers at around 08:30–09:00 UT, which coincides with the second intensification when the SML index reaches a local minimum at 09:12 UT. After

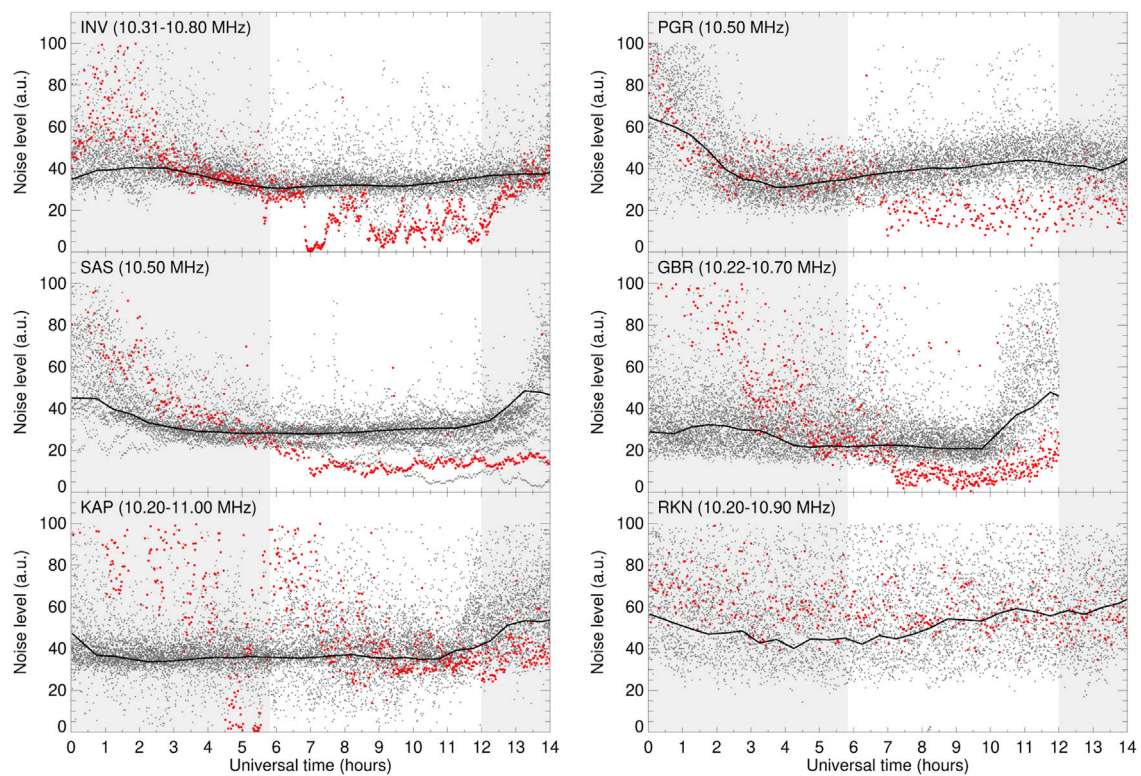


**FIGURE 4**

HF radio noise measurements from six SuperDARN radars in North America. The grey dots show noise measurements for the 21-day period 15 October to 4 November 2019, and the solid black line shows the quiet day curve derived from these data. The red dots show the noise measurements for the event day (25 October 2019). Grey shading indicates time periods before and after the substorm event.

the second intensification, the CNA data become more complicated and there is no obvious relationship between the CNA enhancements at each station.

### 3.2 Atmospheric noise attenuation

Estimates of the atmospheric noise attenuation (ANA) derived from the SuperDARN radars have been used to complement the CNA measurements from Figure 3. Like the CNA, the ANA has been calculated relative to a quiet day curve determined from the noise measurements obtained during the 21-days interval centred on the substorm event date. The 10–11 MHz noise measurements from the six SuperDARN radars in North America that had data available during this period are shown in Figure 4 as a function of universal time. The noise measurements from the entire 21-days interval are shown as grey dots, and the noise measurements from the event date are shown as red dots. The radar data analysis software estimates the noise level as the mean of the 10 lowest power measurements along the beam, and then a correction for the effective number of noise samples is applied (Ponomarenko et al., 2022). The

resulting noise estimates have arbitrary units that vary widely from radar-to-radar, so the data shown in Figure 4 have been scaled to the range 0–100 a.u. to simplify the presentation of the results.

To determine the QDC for each radar, we first divided the noise measurements into 30min bins of universal time. In each time bin we calculated a probability distribution function (PDF) of the noise, and the noise level corresponding to the maximum of that PDF was selected as the quiet day value in that time bin. The quiet day values were then smoothed in time using a boxcar filter of width 2-h to obtain the final QDC, which is the solid black line shown in Figure 4. Although each radar samples in 16 different directions, for simplicity we have used data from only a single beam from each radar in this study. During the period 15 October to 4 November, many of the radars operated with a reduced number of beams in order to sample at a higher time resolution. Therefore, we used the beam with the largest amount of available data during the 21-days reference period, which was beam 12 for the GBR radar and beam 5 for all other radars. To avoid biasing the quiet day curve towards the dates with high time resolution measurements, all data were downsampled to a time resolution of 1 min before determining the QDC. No usable

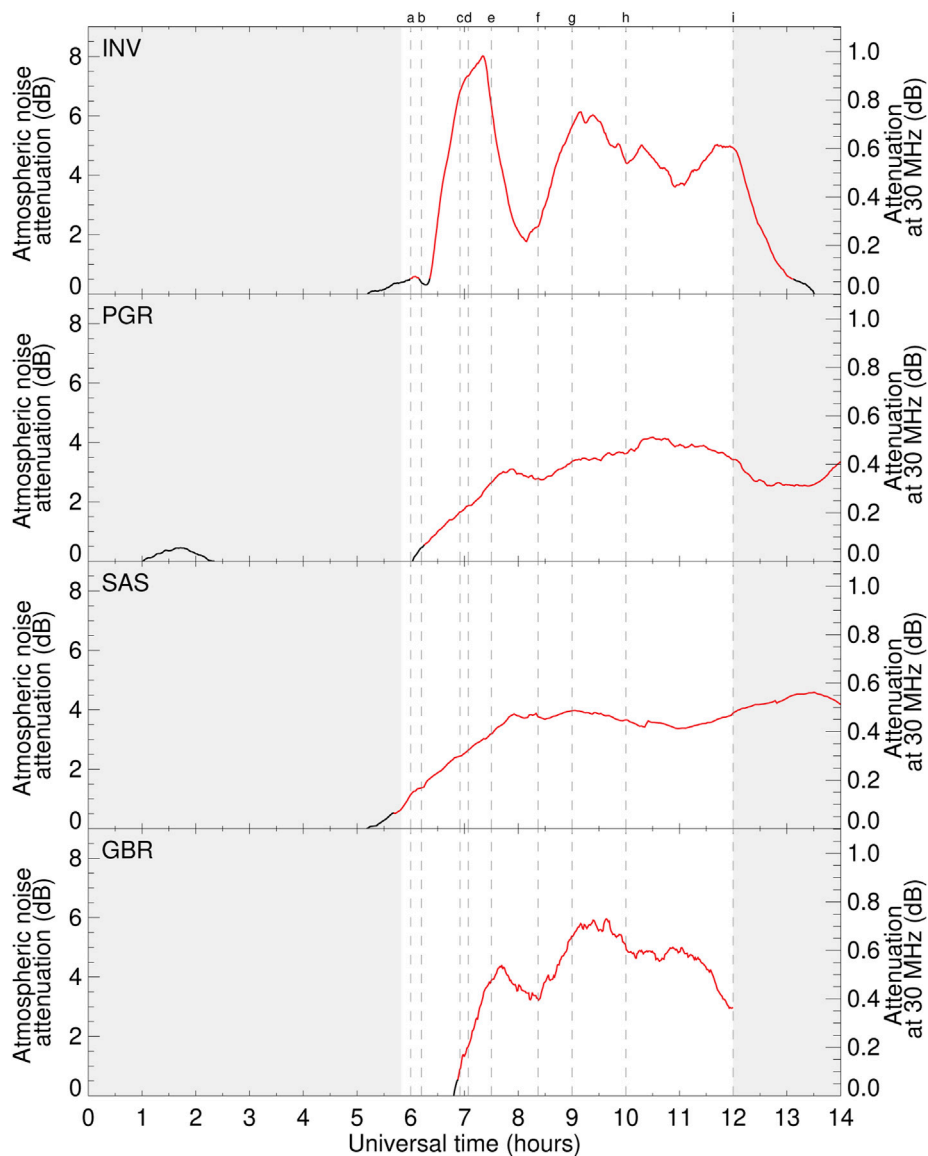


**FIGURE 5**

Atmospheric noise attenuation (ANA) estimates for the Inuvik (INV), Prince George (PGR), Saskatoon (SAS) and Goose Bay (GBR) SuperDARN radars on 25 October 2019. The left axis shows the ANA values at the native radar operating frequency. The right axis shows the equivalent attenuation at 30 MHz (see text for details). The vertical dashed lines correspond to the time intervals shown in Figure 7.

data were available from the GBR radar after 12:00 UT, since the radar switched to a different operating frequency at that time each day.

The grey shading in Figure 4 indicates the time periods before and after the substorm on 25 October 2019. For all radars except KAP and RKN, the noise measurements during the substorm are much lower than the reference level (QDC), indicating that the 10–11 MHz radio noise was attenuated during the event. This is especially clear for the INV radar, where the noise level decreases sharply just before 07:00 UT. In all six panels, there are times when the noise values on the

event day are much higher than the QDC, which may be evidence of interference from other HF emitters. For example, the noise levels on the event day (red dots) at INV and GBR clearly exceed the quiet day values from about 00:00–03:00 UT, making the data unreliable at this time. We also note that the KAP and RKN datasets appear to be dominated by external interference. For KAP, the noise measurements from the event day are distributed well above the quiet day curve from 00:00–07:30 UT. For RKN, the noise data have large variability for the entire 21-day period, including the event day. We conclude that the KAP

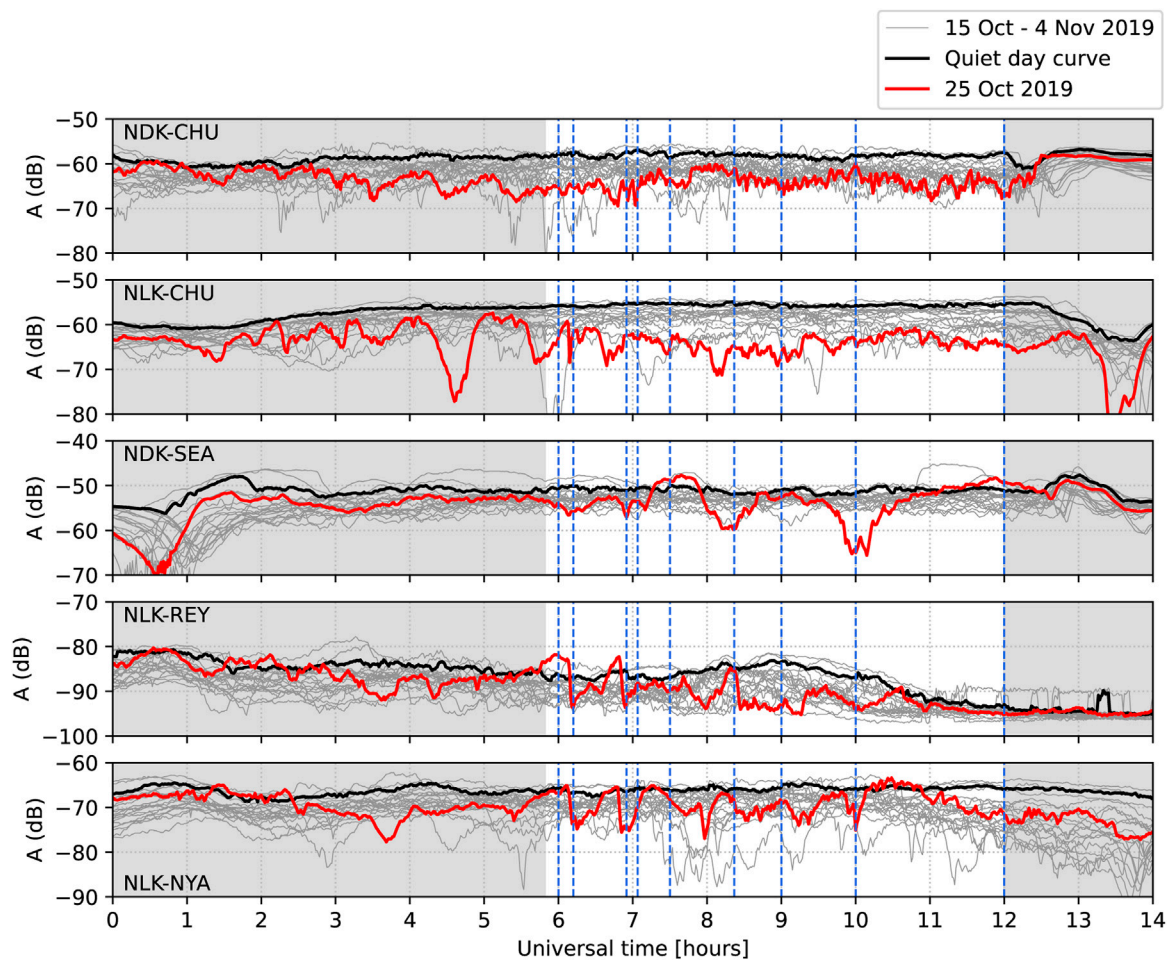


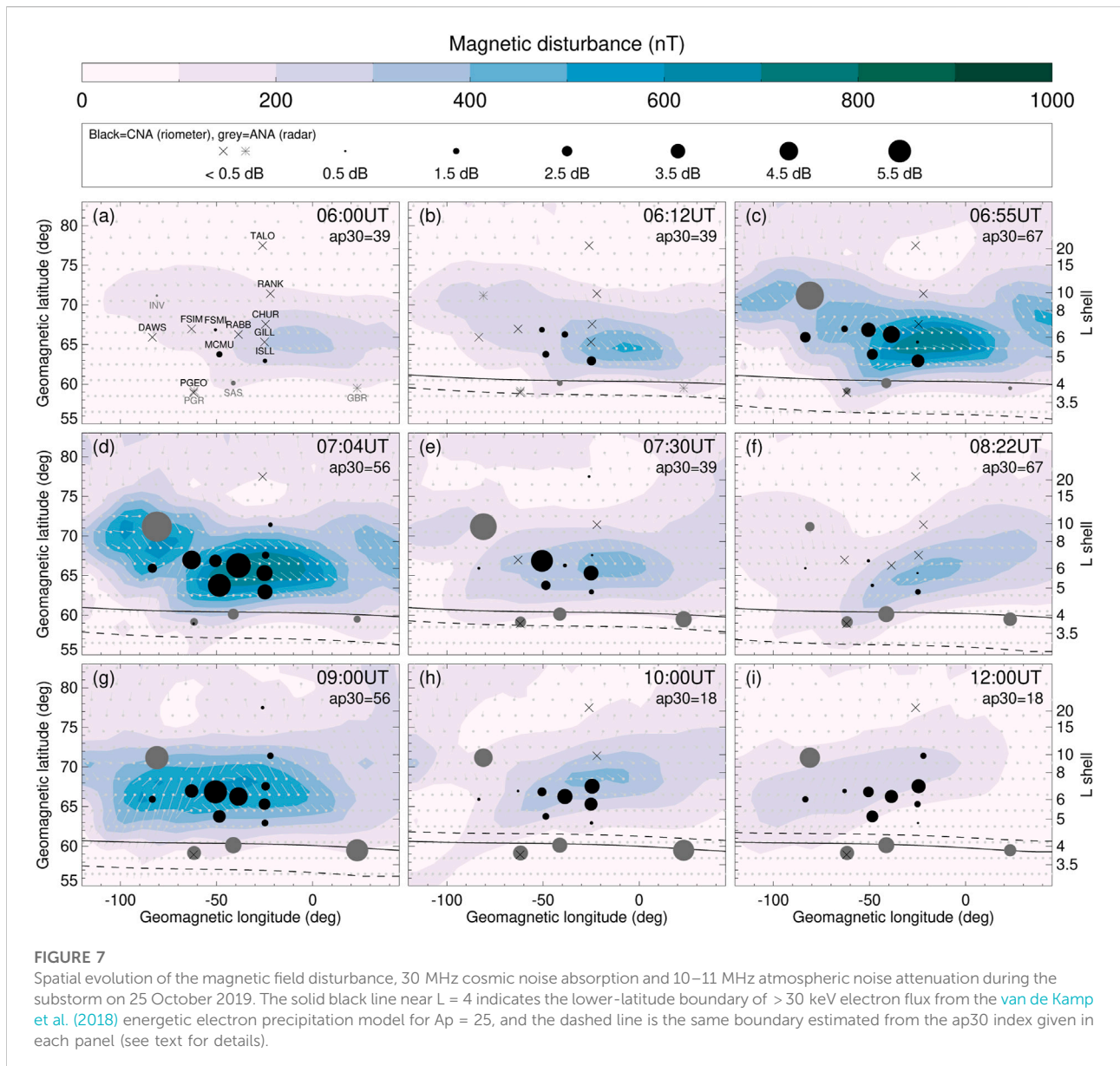
**FIGURE 6**

Amplitude variation of narrowband VLF observations corresponding to the NDK–Churchill (CHU), NLK–Churchill, NPM–Churchill, NLK–Reykjavik (REY) and NLK–Ny Álesund (NYA) propagation paths. The red line shows the data from the event day (25 October 2019) and the grey lines show data from the 21-day period 15 October to 4 November 2019. The quiet day curve is shown in black. The white shading indicates the substorm event. The blue dashed lines correspond to the time instants shown in Figure 7.

and RKN data cannot be used to obtain a reliable estimate of the ANA during this time period and we exclude these data from further analysis.

ANA estimates at 10–11 MHz for the INV, PGR, SAS and GBR radars on 25 October 2019 are shown in Figure 5. These values were calculated relative to each radar’s QDC using Eq. 1 and then smoothed using a boxcar filter of width 1 h. Following the format of Figure 3, ANA values above our chosen threshold value of 0.5 dB are coloured red. We also show the equivalent attenuation at the riometer operating frequency at 30 MHz using the right vertical axis. This was determined by assuming an inverse square relationship between frequency and attenuation (e.g., Milan et al., 2008). However, it is clear from Figures 3, 5 that this scaling procedure does not produce comparable CNA/ANA magnitudes, and the time evolution of the CNA and

ANA datasets is also very different. In particular, only the INV radar observes distinct ANA peaks at 07:00 UT and 09:00 UT, in contrast to the CNA which includes clearly discernible peaks at these times at most riometer stations. The PGR, SAS and GBR radars observe a steady increase in ANA that does not recover during the time interval shown. The co-located PGR radar and PGEO riometer also observe very different responses to the EEP. While the radar measured a clear increase in ANA at the beginning of the event that persisted to the end of the recovery phase, the PGEO riometer did not detect any CNA above the threshold level except for a brief enhancement at 07:00 UT. These results indicate that the SuperDARN radars may be sensitive to lower EEP fluxes than the riometers, or they may be sensitive to different parts of the precipitating energy spectrum.



### 3.3 Sub-ionospheric very low frequency propagation

[Figure 6](#) shows the amplitude variations for the five VLF transmitter–receiver paths that were shown in the inset of [Figure 1](#). The thin grey lines show the amplitude measurements for the reference period 15 October to 4 November 2019, and the upper envelope (90th percentile) of these data is used as the quiet day curve (black line). The VLF amplitudes during the reference period exhibit substantial day-to-day variability, reflecting the reduced stability of the lower ionosphere on the nightside ([Thomson et al., 2007](#)). The data for the substorm event day are shown in red. Substorm EEP causes

decreases in the VLF amplitude (increase in phase) ([Clilverd et al., 2008](#)), and several such amplitude decreases can be identified in [Figure 6](#) relative to the QDC. The NLK–CHU, NLK–REY and NLK–NYA pairs all detect a sharp amplitude decrease near the substorm onset at  $\sim 06:10$  UT. A more gradual amplitude decrease is observed by the NDK–SEA pair at the substorm onset. In all cases the amplitude recovers well before the maximum magnetic field disturbance at 07:04 UT. Just before 07:00 UT, another amplitude decrease is observed by the NLK–REY and NLK–NYA pairs, which both recover within about 15–20 min. Amplitude decreases are also observed by all station pairs during the second expansion phase (07:45–09:12 UT). A final amplitude decrease occurs at around 10:00 UT at

NDK-SEA, NLK-REY and NLK-NYA, indicating an enhancement in the ~50–200 keV electron flux well into the second recovery phase when the magnetic indices have already recovered.

### 3.4 Energetic electron precipitation spatial extent

Now that we have determined the responses of the ground-based instruments to the substorm EEP, we can visualise the spatial coverage and evolution of the EEP impact area. We focus initially on the CNA and ANA responses, and then return to the VLF dataset. [Figure 7](#) shows the CNA, ANA and horizontal magnetic field disturbance at nine time intervals during the substorm. The filled contours show the magnitude of the total horizontal magnetic field disturbance, and the grey vectors indicate the direction of the ionospheric equivalent current obtained by rotating the horizontal magnetic field perturbation direction clockwise by 90°. The filled circles in each panel show the CNA (black) and ANA (grey) measured by the riometers and radars respectively. Cross/star symbols are used when the CNA/ANA is below the threshold value of 0.5 dB. The CNA and ANA measurements have been averaged over a 6-min time window centered on the time stamp shown on each panel. To remove the effect of the apparent offset in the ISLL riometer data, 1.3 dB has been subtracted from all ISLL measurements shown in the figure. In addition, we completely exclude the KAP and RKN radar observations since we have concluded they are unreliable. All other observations shown match the time series data presented in [Figures 3, 5](#). Due to the different operating frequencies of the riometers and SuperDARN radars, it is not appropriate to compare the CNA and ANA magnitudes.

The results in panels (a) and (b) show that the initial CNA enhancement associated with the substorm injection is confined to a narrow region between approximately 63° and 67° CGM latitude. At 06:55 UT (panel c), the magnetic disturbance increases and CNA/ANA enhancements are measured over a wider longitudinal and latitudinal area, reaching a maximum spatial coverage and magnitude at 07:04 (panel d). The TALO riometer was the only instrument that did not detect any EEP signature at 07:04 UT, indicating that the EEP impact area was confined to latitudes below 77° CGM at this time. However, the TALO riometer detected a brief CNA enhancement shortly afterwards, which is evident in panel (e) and also in [Figure 3](#).

Panels (e) and (f) show the response of each instrument during the first recovery phase. As expected, the CNA/ANA gradually decrease across most of the observable area as the magnetic field disturbance weakens. The three SuperDARN radars at the equatorward edge of the observable area (~58–60° CGM latitude) continue to detect ANA above the threshold level at 08:22 UT, and the INV radar measures

about 2 dB ANA at ~70° CGM latitude. At the same time, all CNA measurements are close to or below the threshold value.

Panel (g) shows the CNA/ANA response during the second intensification of the substorm. The magnetic field disturbance is accompanied by a CNA/ANA enhancement across the entire observable area. The PGEO riometer did not detect CNA above the threshold level, but there is a clear ANA response from the co-located SuperDARN radar (PGR). The enhanced CNA/ANA continues into the substorm recovery phase (panels h–i) at all sites except the highest-latitude riometer (TALO). We note that a substantially higher CNA response was measured during the final recovery phase (panels h–i) compared to the first recovery phase (panel f), even though the magnetic field intensifications preceding them had similar magnitudes. Although not shown in [Figure 7](#), it is evident from [Figures 3, 5](#) that the CNA/ANA enhancements at some sites continue until 14:00 UT, which is 2 h after the end of the final recovery phase and more than 8 h after the substorm onset.

To determine whether the observations presented in [Figure 7](#) provide a reasonable estimate of the EEP impact area, we compare the CNA/ANA results with the vertical total electron content (vTEC) dataset. [Figure 8](#) shows the vTEC data for the same time instants as in [Figure 7](#), with some small differences in timing due to the 5 min resolution of the vTEC dataset. The midlatitude ionospheric trough can be identified in each panel as the electron density depression with wide longitudinal extent that is located equatorward of the riometers. The poleward boundary of the midlatitude trough is associated with the equatorward edge of the auroral oval, and can therefore be used to identify the lower latitude limit of substorm EEP (e.g., [Zou et al., 2011](#)). There is a clear vTEC increase of 2–4 TECu in the northwest at the first intensification (panels c–d) that extends to the approximate locations of the PGR and SAS radars. This matches well with the CNA and ANA enhancements near DAWS and INV, and also the magnetic field enhancement in the equivalent panels of [Figure 7](#). South of the PGR, SAS and GBR radar sites the vTEC is close to zero, indicating that the equatorward edge of the EEP impact area for this event is close to the radar locations. Similarly, the vTEC enhancement extends about as far north as the RANK riometer during the first intensification (panel d), and then further north to TALO during the second intensification (panel g), which matches the CNA observations from these two riometers. Based on this comparison, we conclude that our CNA/ANA measurements provide a reasonable estimate of the latitudinal extent of the EEP impact area for this substorm. The enhanced vTEC over Alaska indicates the EEP impact area may extend much further westward of the area observable by the riometers and radars.

The green lines in [Figure 8](#) show the propagation paths between the VLF transmitter–receiver pairs. A solid line is used if the amplitude  $A_{VLF}$  meets the criterion  $A_{VLF} < A_{QDC} - 2A_{\sigma}$ , where  $A_{QDC}$  is the value of the QDC and  $A_{\sigma}$  is the standard deviation of the amplitude measurements over the 21-days

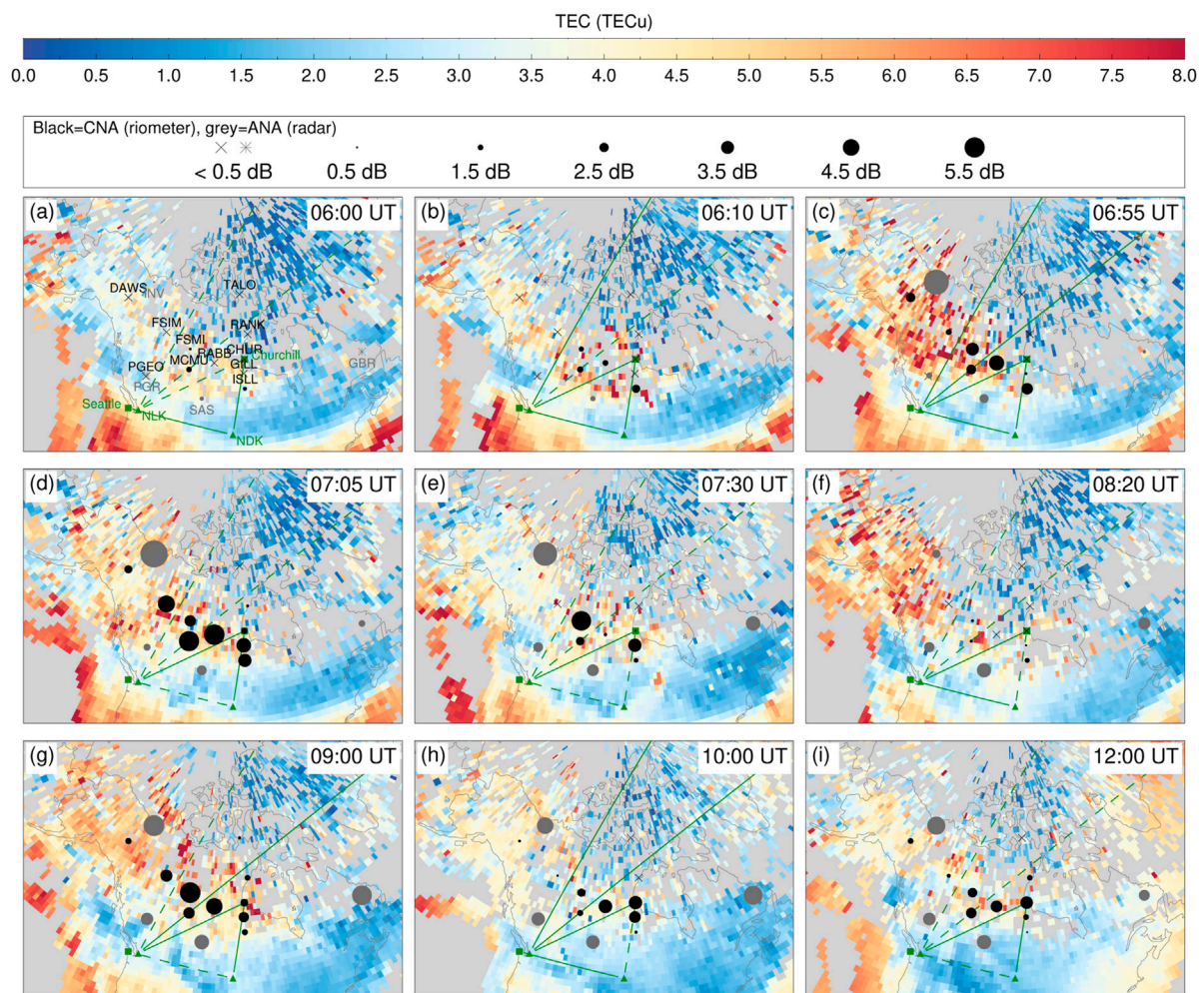


**FIGURE 8**

Spatial evolution of the vertical total electron content (vTEC), 30 MHz cosmic noise absorption, and 10–11 MHz atmospheric noise attenuation during the substorm on 25 October 2019. The solid green lines show the VLF propagation paths with a significant amplitude change relative to the reference period, and the dashed green lines indicate VLF propagation paths with no significant amplitude change (see text for details). VLF = very low frequency.

reference period at the corresponding universal time. A dashed line is used if that criterion is not met. All station pairs meet the criterion at 06:55 UT (panel c) when the vTEC enhancements along the propagation paths reach a maximum. The NLK–Churchill pair also meets the criterion from panel b onwards. An important observation is that the amplitude enhancements detected by the low-latitude pair NDK–Seattle coincide with vTEC enhancements closer to the receiver station (Seattle), and that there are no vTEC enhancements near the NDK transmitter at any of the times shown. However, it is unclear whether the vTEC enhancement near Seattle is actually related to the substorm EEP, since the Seattle VLF receiver is located equatorward of the midlatitude ionospheric trough identified in the vTEC dataset throughout the event.

Existing statistical descriptions of EEP flux can be used to put the spatial extent of the EEP during this substorm into a broader context, in particular the latitudinal extent of the EEP. [Cresswell-Moorcock et al. \(2013\)](#) showed that equatorward edge of the EEP flux above 30 keV during an average substorm occurs at  $L = 4.6 \pm 0.2$ , and at  $L = 4.1 \pm 0.1$  for the strongest 25% of substorms in their dataset, where the strength of an event was defined by the EEP flux. Their latitudinal extent results were similar to the earlier statistical study of  $>0.3$  dB CNA during substorms by [Berkey et al. \(1974\)](#). For our case study, the SuperDARN radars detected evidence of EEP at  $L = 3.7$ – $4.0$ , indicating that the EEP impact area extended *at least* this far equatorward and possibly further. No satellite EEP flux measurements were available for our case study event, but the moderate geomagnetic conditions ( $18 \leq ap30 \leq 67$ ) suggest that the EEP fluxes could easily be

within the upper quartile range of the [Cresswell-Moorcock et al. \(2013\)](#) event list.

The  $A_p$ -dependent EEP flux model by [van de Kamp et al. \(2018\)](#) provides another helpful comparison with our case study. This model provides median electron fluxes above 30 keV as a function of the daily geomagnetic index  $A_p$ , the L-value, and the magnetic local time (MLT). The [van de Kamp et al. \(2018\)](#) model includes all EEP flux above 30 keV, including from non-substorm activity, but we expect that most of the EEP is associated with substorm processes ([Nesse Tysøy et al., 2021](#)). We have estimated the latitude limits of the EEP as the L-value at which the modelled  $> 30$  keV electron flux falls below  $2000 \text{ cm}^{-2} \text{ s}^{-1} \text{ sr}^{-1}$  using the equations for the MLT-dependent model described in [Section 3.2](#) of [van de Kamp et al. \(2018\)](#). The modelled EEP flux decays sharply at the lower latitude limit, so the lower latitude limit of the EEP is not overly sensitive to our choice of flux threshold. In contrast, the EEP flux decays more gradually at the poleward edge of the EEP impact area, so it is more difficult to choose a specific L-value as the poleward extent of the EEP. Therefore, we focus only on the lower latitude limit when comparing our results to the [van de Kamp et al. \(2018\)](#) model. The solid black line near  $L = 4$  in [Figure 7](#) shows the equatorward boundary of the EEP predicted by the model, with  $A_p = 25$  for 25 October 2019. As mentioned already, the SuperDARN radars at  $L = 3.7\text{--}4$  detect a clear ANA response throughout the substorm, indicating the EEP boundary extends at least as far equatorward as  $L = 3.7\text{--}4$ , and probably further. Noting that the  $A_p$  index represents only a daily average of the geomagnetic activity, it is not surprising that the observed EEP impact area extends further equatorward than predicted by the model, since  $ap30$  is well above the daily average during the actual event (up to  $ap30 = 67$ ). The dashed lines in [Figure 7](#) show the modelled position of the equatorward EEP boundary determined using the 30 min  $ap30$  index rather than the daily  $A_p$ . With the  $ap30$  model input, the equatorward EEP boundaries in panels c–g are positioned equatorward of the ANA response and therefore consistent with the observations. In the final recovery phase when  $ap30$  decreases to below the daily average (panels h–i), using  $ap30$  as the model input shifts the EEP boundary to higher latitudes. This further underestimates the size of the EEP impact area during the substorm recovery phase compared to the  $A_p$  model input (solid lines).

## 4 Two additional substorms

To further investigate the extent to which the  $A_p$  and  $ap30$  indices capture the EEP spatial extent, we present two further examples of substorms that occurred during lower geomagnetic activity conditions. The riometer and radar data were processed in the same manner as the previous example, using the 21-days window centred on each event date to determine the quiet day curve.

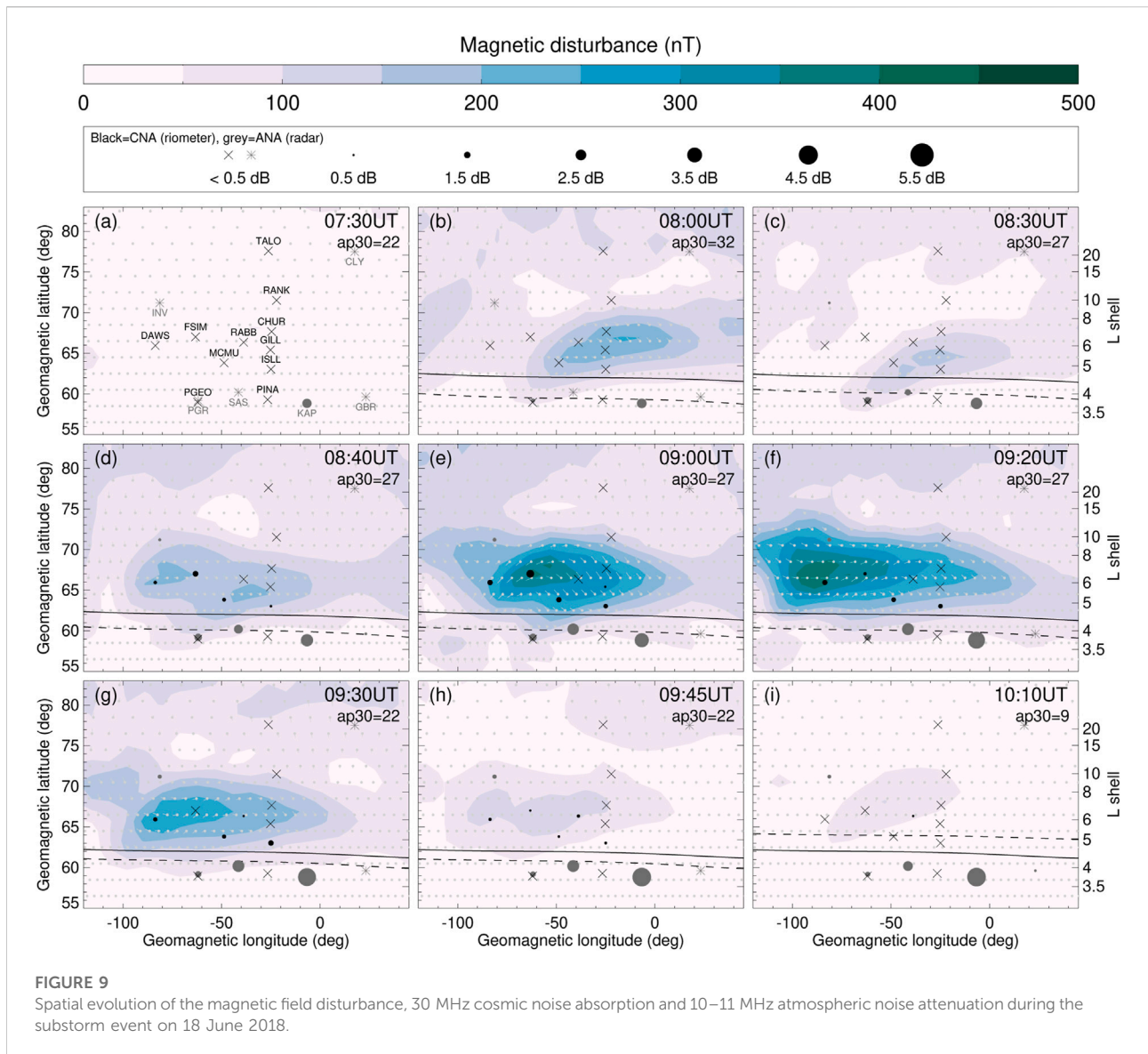
### 4.1 18 June 2018

Maps of the CNA/ANA at nine time instants for a substorm that occurred on 18 June 2018 are shown in [Figure 9](#). This substorm consists of a single expansion–recovery phase pair and the maximum magnetic disturbance of  $\leq 450$  nT is considerably weaker than the event already presented. For this event, data from the Pinawa (PINA) riometer and the Clyde River (CLY) and Kapuskasing (KAP) SuperDARN radars were also available, which extends the observable area towards the northeast and the south. Throughout the event, the CNA did not exceed 2 dB, and the CNA gradually decreased to below the threshold value of 0.5 dB during the recovery phase (panels g–i). No CNA enhancement was observed by the PGEO or PINA riometers near  $L = 4$ , however we note that CNA up to 0.4 dB was measured at PINA (not shown), which is only slightly below the threshold value. In contrast, ANA enhancements were detected by all four SuperDARN radars near  $L = 4$  (PGR, SAS, KAP and GBR), which commenced near the event onset (panel b) and were still present at the end of the substorm recovery phase (panel i). The  $A_p$  index for 18 June 2018 is 16, which places the equatorward edge of the  $> 30$  keV electron flux at about  $L = 4.3\text{--}4.7$  based on the [van de Kamp et al. \(2018\)](#) model. This is shown by the solid black line in each panel of [Figure 9](#). This model prediction is consistent with the absence of CNA at  $L = 4$ , but the SuperDARN measurements indicate that some type of EEP is present at lower latitudes. When  $ap30$  is used as the model input, the low latitude EEP boundary (dashed line) is still poleward of the ANA enhancement measured by the SuperDARN radars. Therefore, neither the  $A_p$  or  $ap30$  model inputs capture the spatial extent of the EEP observed near  $L = 4$  for this substorm.

### 4.2 10 December 2018

Our final case study, presented in [Figure 10](#), shows the EEP spatial coverage during a substorm on 10 December 2018 ( $A_p = 10$ ). Like the 18 June 2018 event, this substorm consists of a single expansion–recovery phase pair. Throughout the event, the CNA and ANA enhancements are confined to  $L \geq 5$ . This agrees with the [van de Kamp et al. \(2018\)](#) model, which places the EEP impact area at  $L \geq 5$  for  $A_p = 10$  (black solid line). There is a small ANA enhancement at PGR in panels (d)–(e), but no other instruments near  $L = 4$  detected any EEP signatures above the threshold level. Based on these observations, it appears that the [van de Kamp et al. \(2018\)](#) model with the  $A_p$  index input provides a good estimate of the low latitude boundary of the EEP for this substorm. The modelled boundary determined from the  $ap30$  index is further equatorward (dashed line), and the observations do not suggest that the EEP extends that far equatorward.

Also apparent in [Figure 10](#) is a clear ANA enhancement at the poleward edge of the observable area. This is observed by the

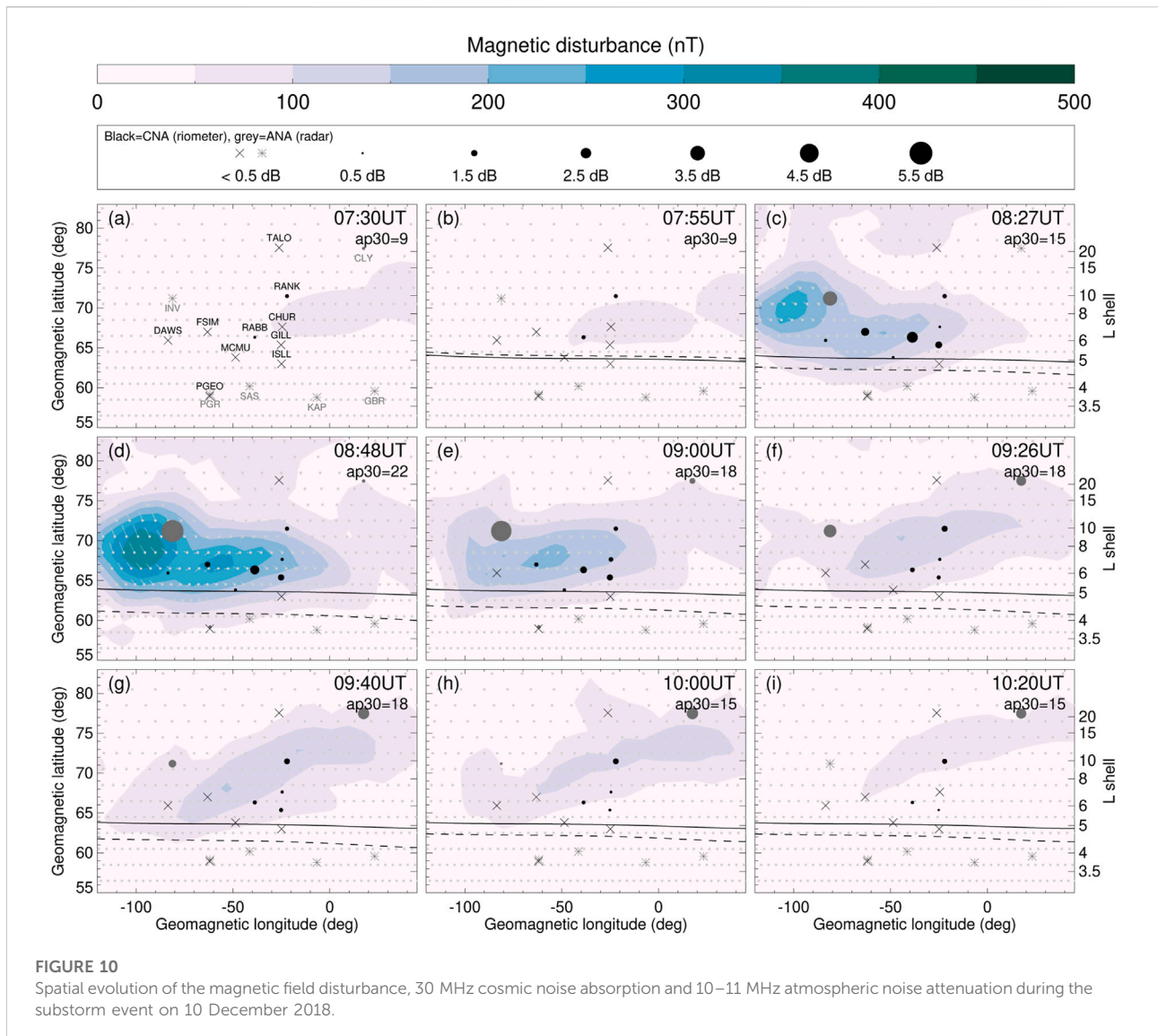


INV radar commencing at 08:27 UT (panel c) and continuing until just after 10:00 UT (panels h–i). Similar behaviour in the CNA is measured by the RANK riometer further to the east. This CNA enhancement does not extend as far north as TALO, but there is an ANA enhancement even further east at CLY from 08:48 UT (panel d) onwards at the northeast edge of the observable area. This is considerably poleward of the EEP boundary of  $L = 14.5 \pm 2$  reported by Cresswell-Moorcock et al. (2013) for an average-type substorm.

## 5 Discussion

In this study we have combined several types of ground-based instruments to estimate the EEP impact area during three

substorms that occurred during low to moderate geomagnetic conditions. The case studies demonstrate that substorm EEP can extend considerably equatorward or poleward of the average latitude limits determined in two earlier studies, Cresswell-Moorcock et al. (2013) and van de Kamp et al. (2018). The evidence for this extended latitude range comes from the atmospheric noise attenuation (ANA) estimates from the SuperDARN radars, and the position of the low-latitude EEP boundary is also supported by the  $v\text{TEC}$  and VLF amplitude observations. We have also shown that the riometers and radars may detect CNA and ANA enhancements throughout the substorm recovery phases. It is likely that these EEP signatures are caused by pulsating aurora (PsA), which are a very common feature of the substorm recovery phase. The latitudinal extent of the recovery phase EEP is well within the



latitude limits reported in our earlier SuperDARN study of ANA during pulsating aurorae (PsA) (Bland et al., 2021). That study showed that the spatial extent of ANA during PsA in the southern hemisphere regularly extends equatorward of 59° CGM latitude and occasionally equatorward of 40° CGM latitude. It is important to note that the recovery phase EEP signatures observed in the CNA, ANA, VLF amplitude and vTEC data are not captured by the magnetometer data or the geomagnetic indices due to the decay of the substorm current systems during this time. This means that geomagnetic indices are not a suitable proxy for EEP during substorm recovery phases.

Another key result from this study is that the ANA enhancements at  $L = 3.7$ – $4$  were not accompanied by clear CNA responses from the riometers at similar latitudes. For the substorms on 25 October 2019 (Figure 7) and 18 June

2018 (Figure 9), these ANA enhancements commenced at the event onset and persisted to the end of the last recovery phase. The ANA was well above the 0.5 dB threshold and therefore represents a significant attenuation of the 10–11 MHz radio noise compared to the 21-days reference period. Without the radar data, one would conclude from Figure 9 that the EEP impact area never extended as far equatorward as PINA ( $L = 3.8$ ) or as far poleward as CHUR ( $L = 6.9$ ). The radar observations, however, show that the latitudinal range of the EEP during the 18 June 2018 event extended from *at least*  $L = 3.7$  (KAP) to *at least*  $L = 9.6$  (INV). It is possible that the EEP fluxes are too low during these events for many of the riometers to detect any significant amount of CNA, where we have defined ‘significant’ as  $CNA > 0.5$  dB. The lower operating frequency and the different antenna properties of the SuperDARN radars may make them more sensitive to low-flux EEP compared to the riometers.

In this study we have estimated the minimum spatial extent of substorm EEP based on the response measured by several ground-based radio instruments. The presence or absence of EEP at each instrument site was essentially determined by the instrument sensitivity, rather than a fixed  $>30$  keV electron flux threshold, for example. Since CNA and ANA are both height-integrated quantities, the same absorption response measured from the ground could be attributed to many different EEP energy spectra. While there have been some studies examining the relationship between  $>30$  keV flux and CNA (e.g., Rodger et al., 2013), a clear correlation between  $>30$  keV flux and CNA was identified only for relatively high electron fluxes of at least  $10^6$  cm<sup>-2</sup> s<sup>-1</sup> sr<sup>-1</sup>, which corresponds to about 1 dB of CNA. Our results show that the EEP spatial extent can be much larger than the region in which  $>1$  dB of CNA was measured, so it is difficult to estimate what EEP fluxes might be occurring at the equatorward edge of the EEP impact area where the SuperDARN radars detected significant ANA.

Our estimates of the latitude limits of the EEP impact area rely heavily on a novel EEP detection method (ANA from SuperDARN radars). It is therefore necessary to discuss the uncertainties in the ANA observations and the instrumental differences between the riometers and radars that may contribute to this result. Our earlier work demonstrates that SuperDARN radars can detect ANA associated with energetic proton precipitation (Bland et al., 2018) as well as low-flux EEP associated with pulsating aurora (Bland et al., 2019; Bland et al., 2021), which represent two spectral extremes of energetic particle precipitation. However, the sensitivity of the SuperDARN radars to different EEP spectra has not yet been studied in detail. We expect that the amount of attenuation depends on the electron density and electron-neutral collision frequency, so that the height of maximum attenuation should be the same for radars and riometers. The radars and riometers would therefore be sensitive to the same EEP energies. However, the minimum electron fluxes required to produce a measurable amount of absorption is likely to be different for riometers and radars. As mentioned above, the lower operating frequency of the SuperDARN radars compared to the riometers may make them more sensitive to lower EEP fluxes, which would account for the different instrument responses to the EEP. The width and oblique orientation of the radar beams, and the presence of backlobes and sidelobes in the beam patterns, may also contribute to the differences observed between the radar and riometer datasets. All of these factors require further investigation to make it possible to perform quantitative comparisons between the radar and riometer datasets.

Another important aspect of the radar dataset is the difficulty in assigning geomagnetic coordinates to the ANA measurements. In Figure 7 we have used the radar site as the location of the ANA, but in reality the D-region sampled by each radar is about 2–3° poleward of the radar site (see radar fields of view in Figure 1). We have chosen to display the ANA measurements at the actual

radar locations because the phased-array design of SuperDARN radars results in a large backlobe in the beam pattern, effectively creating a second field of view behind the radar (Milan et al., 1997). The noise measurements from the radars are therefore a superposition of the noise measured in the front and rear fields of view. The  $\nu$ TEC data presented in Figure 8 indicate that the poleward edge of the midlatitude ionospheric trough is very close to the PGR and SAS radar sites, which suggests that the EEP region is likely to be poleward of the radar site for the 25 October 2019 substorm. This means that the ANA measured at these two sites can probably be attributed to the front fields of view shown in Figure 1.

Although more work is required to properly understand what EEP energies and fluxes the SuperDARN radars are sensitive to, our results indicate that EEP with sufficient flux to attenuate 10–11 MHz radiowaves by  $\sim 5$  dB reaches latitudes well equatorward of the model predictions for  $>30$  keV electron flux. This is an important consideration for studying auroral absorption for space weather applications, where the detailed spatial and temporal evolution of the EEP provides important information to HF radio communicators. The long-term atmospheric chemical response to EEP is probably less sensitive to an underestimated EEP impact area because the ozone depletion associated with NO<sub>x</sub> catalysts is confined to the polar vortex (Verronen et al., 2021). Based on this, we expect that the EEP near L = 4 would contribute to NO<sub>x</sub>-related ozone depletion only when the polar vortex is present at these latitudes. Short-term mesospheric ozone depletion caused by HO<sub>x</sub> catalysts occurs independently of the polar vortex location, so accurate knowledge of the EEP impact area would still be required to properly determine the atmospheric response.

## 6 Conclusion

The spatial coverage of the EEP impact area during three substorms has been determined using a combination of riometers, SuperDARN radars, VLF receivers and  $\nu$ TEC measurements in North America. Our results show that substorm EEP can extend considerably equatorward and poleward of the average latitude limits reported in previous studies. Evidence of this extended latitude range was provided by atmospheric noise attenuation (ANA) estimates from SuperDARN radars and from amplitude variations measured by the VLF receivers, which extended the total observable area provided by the riometer network. For our main case study, these datasets indicated that the lower latitude limit of EEP extended at least as far equatorward as L = 3.7–4, but this was not accompanied by a CNA enhancement from the riometer at the same latitude (PGeo). This result reveals a limitation of using 30 MHz CNA measurements to estimate auroral absorption, since the riometers and radars respond differently to the substorm EEP. Further work is required to determine what

EEP energies and fluxes the SuperDARN radars are sensitive to at 10–11 MHz, and to determine how the SuperDARN ANA measurements can be quantitatively compared to the 30 MHz CNA. The wider latitude limits of EEP reported in this study are unlikely to have significant consequences for modelling the long-term atmospheric response to EEP, since the polar vortex already sets a stricter limit on the spatial extent of the NO<sub>x</sub>-related atmospheric response. However, accurate knowledge of the EEP spatial extent would be necessary for modelling the short-term atmospheric response to EEP and for studying auroral absorption. We therefore highlight the potential of the SuperDARN, AARDDVARK and vTEC datasets to help refine our understanding of EEP by extending the area over which EEP can be detected from the ground.

## Data availability statement

Publicly available datasets were analyzed in this study. This data can be found here: The raw data from the Canadian riometers are available from the University of Calgary Space Physics Data portal ([https://data-portal.phys.ucalgary.ca/go\\_rrio](https://data-portal.phys.ucalgary.ca/go_rrio)). SuperDARN data are published in the Federated Research Data Repository (<https://www.frdr-dfdr.ca/repo/collection/superdarn>). The total electron content data are available at [https://w3id.org/cedar?experiment\\_list=experiments4/2019/gps/25oct19&file\\_list=gps191025g.002.hdf5](https://w3id.org/cedar?experiment_list=experiments4/2019/gps/25oct19&file_list=gps191025g.002.hdf5). The VLF data are available at the British Antarctic Survey Polar Data Centre (<http://psddb.nerc-bas.ac.uk/data/access/coverage.php?menu=1,7&class=232&bc=1>). The SuperMAG MLT-Mlat gridded magnetic field data are available at <https://supermag.jhuapl.edu/mag> and the SML indices are available at <https://supermag.jhuapl.edu/indices>. The ap30 and ap indices are available at <https://doi.org/10.5880/Hpo.0002> and <https://doi.org/10.5880/Kp.0001> respectively.

## Author contributions

EB performed the riometer and radar data analysis. TB analysed the VLF data. NP assisted with selecting the case study events. EB wrote the first draft of the manuscript, and

all authors contributed to the manuscript revision and approved the submitted version.

## Funding

EB is supported by the Norwegian Research Council (NRC) under contract 287427. NP is supported by the NRC under CoE contract 223252.

## Acknowledgments

The authors gratefully acknowledge the SuperMAG collaborators (<https://supermag.jhuapl.edu/info/?page=acknowledgement>). The authors acknowledge the use of SuperDARN data. SuperDARN is a collection of radars funded by the national scientific funding agencies of Australia, Canada, China, France, Japan, Norway, South Africa, United Kingdom, and United States. TB wishes to thank Mark Clilverd and Péter Steinbach for the helpful discussions related to narrowband VLF measurements and all operators of the AARDDVARK for maintaining the network. The Go-Canada riometer array is operated by the University of Calgary with financial support from the Canadian Space Agency.

## Conflict of interest

The authors declare that the research was conducted in the absence of any commercial or financial relationships that could be construed as a potential conflict of interest.

## Publisher's note

All claims expressed in this article are solely those of the authors and do not necessarily represent those of their affiliated organizations, or those of the publisher, the editors and the reviewers. Any product that may be evaluated in this article, or claim that may be made by its manufacturer, is not guaranteed or endorsed by the publisher.

## References

- Berkey, F. T., Driatskiy, V. M., Henriksen, K., Hultqvist, B., Jelly, D. H., Shchuka, T. I., et al. (1974). A synoptic investigation of particle precipitation dynamics for 60 substorms in IQSY (1964–1965) and IASY (1969). *Planet. Space Sci.* 22, 255–307. doi:10.1016/0032-0633(74)90028-2
- Bland, E. C., Heino, E., Kosch, M. J., and Partamies, N. (2018). SuperDARN radar-derived HF radio attenuation during the September 2017 solar proton events. *Space* 16, 1455–1469. doi:10.1029/2018SW001916
- Bland, E., Tesema, F., and Partamies, N. (2021). D-region impact area of energetic electron precipitation during pulsating aurora. *Ann. Geophys.* 39, 135–149. doi:10.5194/angeo-39-135-2021
- Bland, E. C., Partamies, N., Heino, E., Yukimatu, A. S., and Miyaoka, H. (2019). Energetic electron precipitation occurrence rates determined using the Syowa East SuperDARN radar. *JGR. Space Phys.* 124, 6253–6265. doi:10.1029/2018JA026437

- Chisham, G., Lester, M., Milan, S. E., Freeman, M. P., Bristow, W. A., Grocott, A., et al. (2007). A decade of the super dual auroral radar network (SuperDARN): Scientific achievements, new techniques and future directions. *Surv. Geophys.* 28, 33–109. doi:10.1007/s10712-007-9017-8
- Clilverd, M. A., Rodger, C. J., Brundell, J., Bähr, J., Cobbett, N., Moffat-Griffin, T., et al. (2008). Energetic electron precipitation during substorm injection events: High-latitude fluxes and an unexpected midlatitude signature. *J. Geophys. Res.* 113, A10311. doi:10.1029/2008JA013220
- Clilverd, M. A., Rodger, C. J., Thomson, N. R., Brundell, J. B., Ulich, T., Lichtenberger, J., et al. (2009). Remote sensing space weather events: Antarctic-radiation-belt (dynamic) deposition-vlf atmospheric research consortium network. *Space 7*, S04001. doi:10.1029/2008SW000412
- [Dataset] Coster, A. (2019). Data from the cedar madrigal database. MIT/Haystack Observatory.
- Cresswell-Moorcock, K., Rodger, C. J., Kero, A., Collier, A. B., Clilverd, M. A., Häggström, I., et al. (2013). A reexamination of latitudinal limits of substorm-produced energetic electron precipitation. *J. Geophys. Res. Space Phys.* 118, 6694–6705. doi:10.1002/jgra.50598
- Daae, M., Espy, P., Nesse Tysøy, H., Newnham, D., Stadsnes, J., and Søraas, F. (2012). The effect of energetic electron precipitation on middle mesospheric nighttime ozone during and after a moderate geomagnetic storm. *Geophys. Res. Lett.* 39, L21811. doi:10.1029/2012GL053787
- Fang, X., Randall, C. E., Lummerzheim, D., Solomon, S. C., Mills, M. J., Marsh, D. R., et al. (2008). Electron impact ionization: A new parameterization for 100 eV to 1 MeV electrons. *J. Geophys. Res.* 113, A09311. doi:10.1029/2008JA013384
- Gjerloev, J. W., Hoffman, R. A., Sigwarth, J. B., and Frank, L. A. (2007). Statistical description of the bulge-type auroral substorm in the far ultraviolet. *J. Geophys. Res.* 112, A07213. doi:10.1029/2006JA012189
- Gjerloev, J. W. (2012). The SuperMAG data processing technique. *J. Geophys. Res.* 117, A09213. doi:10.1029/2012JA017683
- Greenwald, R. A., Baker, K. B., Dudeney, J. R., Pinnock, M., Jones, T. B., Thomas, E. C., et al. (1995). DARN/SuperDARN: A global view of the dynamics of high-latitude convection. *Space Sci. Rev.* 71, 761–796. doi:10.1007/BF00751350
- Jones, S. L., Lessard, M. R., Rychert, K., Spanswick, E., and Donovan, E. (2011). Large-scale aspects and temporal evolution of pulsating aurora. *J. Geophys. Res.* 116, A03214. doi:10.1029/2010JA015840
- Kellerman, A. C., Shprits, Y. Y., Makarevich, R. A., Spanswick, E., Donovan, E., and Reeves, G. (2015). Characterization of the energy-dependent response of riometer absorption. *J. Geophys. Res. Space Phys.* 120, 615–631. doi:10.1002/2014JA020027
- Mann, I. R., Milling, D. K., Rae, I. J., Ozeke, L. G., Kale, A., Kale, Z. C., et al. (2008). The upgraded CARISMA magnetometer array in the THEMIS era. *Space Sci. Rev.* 141, 413–451. doi:10.1007/s11214-008-9457-6
- [Dataset] Matzka, J., Bronkalla, O., Kervalishvili, G., Rauberg, J., and Yamazaki, Y. (2022). Geomagnetic hpo index. v. 2.0. GFZ Data Services. doi:10.5880/Hpo.0002
- [Dataset] Matzka, J., Bronkalla, O., Tornow, K., Elger, K., and Stolle, C. (2021a). Geomagnetic kp index. v. 1.0. doi:10.5880/Kp.0001
- Matzka, J., Stolle, C., Yamazaki, Y., Bronkalla, O., and Morschhauser, A. (2021b). The geomagnetic kp index and derived indices of geomagnetic activity. *Space 19*, e2020SW002641. doi:10.1029/2020SW002641
- McPherron, R. L., and Chu, X. (2018). The midlatitude positive bay index and the statistics of substorm occurrence. *JGR. Space Phys.* 123, 2831–2850. doi:10.1002/2017JA024766
- Mendillo, M. (2006). Storms in the ionosphere: Patterns and processes for total electron content. *Rev. Geophys.* 44, RG4001. doi:10.1029/2005RG000193
- Milan, S. E., Hosokawa, K., Lester, M., Sato, N., Yamagishi, H., and Honary, F. (2008). D region HF radar echoes associated with energetic particle precipitation and pulsating aurora. *Ann. Geophys.* 26, 1897–1904. doi:10.5194/angeo-26-1897-2008
- Milan, S. E., Jones, T. B., Robinson, T. R., Thomas, E. C., and Yeoman, T. K. (1997). Interferometric evidence for the observation of ground backscatter originating behind the CUTLASS coherent HF radars. *Ann. Geophys.* 15, 29–39. doi:10.1007/s00585-997-0029-y
- Newell, P. T., and Gjerloev, J. W. (2011). Evaluation of SuperMAG auroral electrojet indices as indicators of substorms and auroral power. *J. Geophys. Res.* 116, L2211. doi:10.1029/2011ja016779
- Nesse Tysøy, H., Partamies, N., Babu, E. M., Smith-Johnsen, C., and Salice, J. A. (2021). The predictive capabilities of the auroral electrojet index for medium energy electron precipitation. *Front. Astron. Space Sci.* 8. doi:10.3389/fspas.2021.714146
- Nishitani, N., Ruohoniemi, J. M., Lester, M., Baker, J. B. H., Koustov, A. V., Shepherd, S. G., et al. (2019). Review of the accomplishments of mid-latitude super dual auroral radar network (SuperDARN) HF radars. *Prog. Earth Planet. Sci.* 6, 27–57. doi:10.1186/s40645-019-0270-5
- Partamies, N., Tesema, F., Bland, E., Heino, E., Nesse Tysøy, H., and Kalleid, E. (2021). Electron precipitation characteristics during isolated, compound, and multi-night substorm events. *Ann. Geophys.* 39, 69–83. doi:10.5194/angeo-39-69-2021
- Partamies, N., Whiter, D., Kadokura, A., Kauristie, K., Nesse Tysøy, H., Massetti, S., et al. (2017). Occurrence and average behavior of pulsating aurora. *J. Geophys. Res. Space Phys.* 122, 5606–5618. doi:10.1002/2017JA024039
- Ponomarenko, P. V., Bland, E. C., McWilliams, K. A., and Nishitani, N. (2022). On the noise estimation in super dual auroral radar network data. *Radio Sci.* 57, e2022RS007449. doi:10.1029/2022rs007449
- Randall, C. E., Harvey, V. L., Singleton, C. S., Bailey, S. M., Bernath, P. F., Codrescu, M., et al. (2007). Energetic particle precipitation effects on the southern hemisphere stratosphere in 1992–2005. *J. Geophys. Res.* 112, D08308. doi:10.1029/2006j0007696
- Rideout, W., and Coster, A. (2006). Automated GPS processing for global total electron content data. *GPS Solut.* 10, 219–228. doi:10.1007/s10291-006-0029-5
- Rodger, C. J., Clilverd, M. A., Kavanagh, A. J., Watt, C. E. J., Verronen, P. T., and Raita, T. (2012). Contrasting the responses of three different ground-based instruments to energetic electron precipitation. *Radio Sci.* 47, 1–13. doi:10.1029/2011RS004971
- Rodger, C. J., Kavanagh, A. J., Clilverd, M. A., and Marple, S. R. (2013). Comparison between POES energetic electron precipitation observations and riometer absorptions: Implications for determining true precipitation fluxes. *J. Geophys. Res. Space Phys.* 118, 7810–7821. doi:10.1002/2013JA019439
- Seppälä, A., Matthes, K., Randall, C. E., and Mironova, I. A. (2014). What is the solar influence on climate? Overview of activities during CAWSES-II. *Prog. Earth Planet. Sci.* 1, 24. doi:10.1186/s40645-014-0024-3
- Seppälä, A., Verronen, P. T., Clilverd, M. A., Randall, C. E., Tamminen, J., Sofieva, V., et al. (2007). Arctic and Antarctic polar winter NO<sub>x</sub> and energetic particle precipitation in 2002–2006. *Geophys. Res. Lett.* 34, L12810. doi:10.1029/2007gl029733
- Sergeev, V. A., Shukhtina, M. A., Stepanov, N. A., Rogov, D. D., Nikolaev, A. V., Spanswick, E., et al. (2020). Toward the reconstruction of substorm-related dynamical pattern of the radiowave auroral absorption. *Space 18*, e2019SW002385. doi:10.1029/2019SW002385
- Shepherd, S. G. (2014). Altitude-adjusted corrected geomagnetic coordinates: Definition and functional approximations. *J. Geophys. Res. Space Phys.* 119, 7501–7521. doi:10.1002/2014ja020264
- Sinnhuber, M., Nieder, H., and Wieters, N. (2012). Energetic particle precipitation and the chemistry of the mesosphere/lower thermosphere. *Surv. Geophys.* 33, 1281–1334. doi:10.1007/s10712-012-9201-3
- Smith-Johnsen, C., Marsh, D. R., Orsolini, Y., Nesse Tysøy, H., Hendrickx, K., Sandanger, M. I., et al. (2018). Nitric oxide response to the april 2010 electron precipitation event—Using WACCM and WACCM-D with and without medium energy electrons. *J. Geophys. Res. Space Phys.* 123, 5232–5245. doi:10.1029/2018JA025418
- Spanswick, E., Donovan, E., Friedel, R., and Korth, A. (2007). Ground based identification of dispersionless electron injections. *Geophys. Res. Lett.* 34, L03101. doi:10.1029/2006GL028329
- Spanswick, E., Donovan, E., Liu, W., Liang, J., Blake, J. B., Reeves, G., et al. (2009). Global observations of substorm injection region evolution: 27 august 2001. *Ann. Geophys.* 27, 2019–2025. doi:10.5194/angeo-27-2019-2009
- [Dataset] Super Dual Auroral Radar Network (2021). SuperDARN 2018 RAWACF. doi:10.20383/101.0290
- [Dataset] Super Dual Auroral Radar Network (2022). SuperDARN 2019 RAWACF. doi:10.20383/102.0558
- Tesema, F., Partamies, N., Nesse Tysøy, H., Kero, A., and Smith-Johnsen, C. (2020). Observations of electron precipitation during pulsating aurora and its chemical impact. *JGR. Space Phys.* 125, e2019JA027713. doi:10.1029/2019JA027713
- Thomson, N. R., Clilverd, M. A., and McRae, W. M. (2007). Nighttime

ionospheric D region parameters from VLF phase and amplitude. *J. Geophys. Res.* 112, A07304. doi:10.1029/2007JA012271

Turunen, E., Kero, A., Verronen, P. T., Miyoshi, Y., Oyama, S.-I., and Saito, S. (2016). Mesospheric ozone destruction by high-energy electron precipitation associated with pulsating aurora. *JGR. Atmos.* 121, 11,852–11,861. doi:10.1002/2016JD025015

van de Kamp, M., Rodger, C. J., Seppälä, A., Clilverd, M. A., and Verronen, P. T. (2018). An updated model providing long-term data sets of energetic electron precipitation, including zonal dependence. *J. Geophys. Res. Atmos.* 123, 9891–9915. doi:10.1029/2017JD028253

van de Kamp, M., Seppälä, A., Clilverd, M. A., Rodger, C. J., Verronen, P. T., and Whittaker, I. C. (2016). A model providing long-term data sets of energetic electron precipitation during geomagnetic storms. *J. Geophys. Res. Atmos.* 121, 12, 520–540. doi:10.1002/2015JD024212

Verronen, P. T., Kero, A., Partamies, N., Szelag, M. E., Oyama, S.-I., Miyoshi, Y., et al. (2021). Simulated seasonal impact on middle atmospheric ozone from high-energy electron precipitation related to pulsating aurorae. *Ann. Geophys.* 39, 883–897. doi:10.5194/angeo-39-883-2021

Watson, C., Jayachandran, P. T., Spanswick, E., Donovan, E. F., and Danskin, D. W. (2011). GPS TEC technique for observation of the evolution of substorm particle precipitation. *J. Geophys. Res.* 116. doi:10.1029/2010JA015732

Yamazaki, Y., Matzka, J., Stolle, C., Kervalishvili, G., Rauberg, J., Bronkalla, O., et al. (2022). Geomagnetic activity index hpo. *Geophys. Res. Lett.* 49, e2022GL098860. doi:10.1029/2022gl098860

Zou, S., Moldwin, M. B., Coster, A., Lyons, L. R., and Nicolls, M. J. (2011). Gps tec observations of dynamics of the mid-latitude trough during substorms. *Geophys. Res. Lett.* 38, L14109. doi:10.1029/2011GL048178